Geometric barrier in $Bi_2Sr_2CaCu_2O_{7+\delta}$ single crystals

Leonardo R. E. Cabral,* Clécio C. de Souza Silva, and J. Albino Aguiar
Laboratório de Supercondutividade, Departamento de Física, Universidade Federal de Pernambuco, 50670-901 Recife, Brazil

Ernst Helmut Brandt
Max-Planck-Institut für Metallforschung, D-70506 Stuttgart, Germany
(Received 31 August 2001; published 22 March 2002)

In this paper we present isothermal magnetization curves measured by using a $Bi_2Sr_2CaCu_2O_{7+\delta}$ single crystal in the temperature range 50 K–80 K, for external magnetic fields applied along the sample thickness. The experimental data is compared with the numerically calculated magnetization, in which the specimen geometry is correctly taken into account. In this calculation an explicit equilibrium relation $H=H(B,\tilde{\kappa})$ is also considered, where $\tilde{\kappa}$ is related to the Ginzburg-Landau parameter. The reversible experimental and calculated magnetizations show good agreement, allowing us to estimate $H_{c1}(T)$. The results show that the geometric barrier is mainly responsible for the magnetic hysteresis observed at high temperatures ($T \geqslant 70$ K) where bulk pinning is negligible.

DOI: 10.1103/PhysRevB.65.134514 PACS number(s): 74.60.Ec, 74.60.Ge, 74.60.Jg

I. INTRODUCTION

Type-II superconductors may give rise to hysteresis in the magnetization measured when an external field is cycled. This hysteresis has been usually associated with bulk pinning, as can be shown by the Bean model,[1] and/or with surface barriers such as the Bean-Livingston barrier.[2] Results for critical-state models[1,3] and for surface barriers[4] are well known for external fields parallel to the larger dimension of the sample (parallel field). Recently, computer simulations of the vortex dynamics considering both pinning and surface barriers[5,6] were performed for films in parallel field, based on the London approach.

However, superconducting samples (single crystals and films) are prepared frequently with thicknesses much smaller than the transverse dimensions and the magnetization data is obtained with the external field applied along the sample thickness (perpendicular field) in order to measure large signals. This makes the theoretical interpretation intricate because of the large and nonuniform demagnetization effect that such superconducting samples exhibit. Indeed, it has been shown that the current and magnetic-field profiles of superconductors in perpendicular field differ from those in parallel field.[7,8] Moreover, hysteresis may be observed even in the absence of bulk pinning or Bean-Livingston barriers if a sample with constant thickness is in a perpendicular field. This pin-free irreversibility is caused by the so-called geometric barrier[9–12] against the entrance of magnetic flux, and occurs in samples with nonellipsoidal cross section. Flux can enter only when the shielding current near the specimen edges reaches some threshold value that depends on the sample thickness and determines the entrance field $H_{\rm en}$. Due to the Lorentz force acting on the vortices, the penetrating flux accumulates in the middle of the sample. When the external field is lowered, this dome-shaped field distribution becomes wider, vortices move towards the edges, and there is no barrier for flux exit.

The different dynamics for flux entrance and exit generates magnetization hysteresis. The numerical calculation developed by Brandt[9,13,14] allows us to study this barrier and yields field and current profiles and magnetization curves for superconducting bars and disks of any aspect ratio, with or without bulk pinning.

Another difficulty for understanding high-T_c superconductors such as $Bi_2Sr_2CaCu_2O_{7+\delta}$ (BSCCO-2212) is the fact that they are anisotropic, i.e., the effective electron mass may be different along different crystalline axes. The electron masses along the a and b axes can be taken as equal (m_{ab}) but are much smaller than the mass along the c axis (m_c). This anisotropy makes the superconducting properties quite different when measured in the ab plane or along the c axis. Thermal fluctuations of vortices are enhanced by the anisotropy parameter $\Gamma=\sqrt{m_c/m_{ab}}$,[15] which can reach very high values in BSCCO-2212.[16] For instance, the large decrease in the hysteresis width as the temperature is increased[17] may be related to the thermal fluctuations in these materials.

In this paper we present isothermal magnetization curves taken by using a BSCCO-2212 single crystal and compare these curves with numerically calculated ones. We employed the numerical method developed by Brandt,[9,13,14] including appropriate material relations $E=E(j)$ and $H=H(B)$. Here E is the electric field (generated by moving vortices), j the current density, B the induction, and H the reversible magnetic field that is in equilibrium with B. Unlike previous works,[18,19] here the rectangular cross section of the measured specimen is taken into account. The experimental data was collected at temperatures between 50 K and 80 K. In this temperature range, the hysteresis shows considerable contribution from geometric and/or surface barriers. For instance, the geometric barrier—with negligible bulk critical current—may account for the hysteresis observed at temperatures above 60 K. For temperatures equal to or lower than 60 K, surface barriers, such as the Bean-Livingston barrier, could be acting on this sample. The reversible magnetization $M=B-H$ is well fitted by using the Clem-Hao model[20] for the equilibrium relation $H=H(B)$, with decreasing effective κ

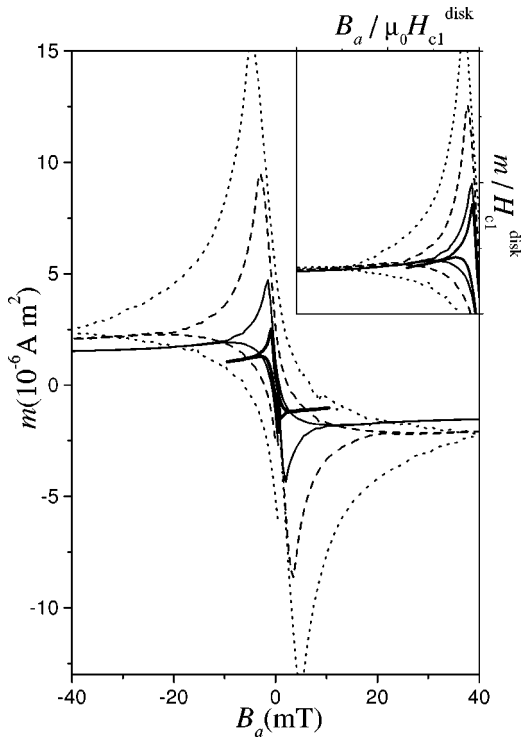

FIG. 1. Measured magnetization loops at $T=50$ K, 60 K, 70 K, and 80 K (dotted, dashed, solid, and thick solid lines, respectively) showing the rapid hysteresis decrease as the temperature is increased. Inset: magnetization and external field normalized by the estimated $H_{c1}^{\rm disk}$ at each temperature. The reversible branches seem to coincide but they do depend on temperature (through the parameter $\tilde{\kappa}$) as shown by direct comparison between numerical and experimental data.

for increasing temperature T, which permits to estimate the lower critical field of this sample.

II. EXPERIMENT

The single crystal was prepared by the flux method[21] and showed a sharp diamagnetic transition at $T_c=90$ K. It is of approximately rectangular shape ($\sim 2.6\times 1.8\text{mm}^2$) with thickness (along c) of about 0.08 mm. The measurements were performed in a quantum design superconducting quantum interference device magnetometer for dc fields applied parallel to the crystal c axis.

The magnetization was measured in the standard way: the sample was cooled from $T \gg T_c$ to the desired temperature (below T_c) at zero external field; after the temperature was established, the sample magnetic moment was measured while the external field was cycled. When the cycle was finished, the sample was warmed up to a temperature well above T_c and the procedure was repeated for another target temperature. Figure 1 depicts the magnetic moment as a function of the external field at $T=50$ K, 60 K, 70 K, and 80 K (outer to inner loop). In the inset we show magnetization and external field normalized by the estimated $H_{c1}^{\rm disk}$ at each temperature (values in Sec. IV). It is noticed that the hysteresis width presents a fast decrease with increasing temperature. Moreover, the hysteresis is asymmetric, i.e., the reversible magnetization is different from zero, indicating that surface and/or geometric barriers may be present. The narrow hysteresis ($\Delta m \sim 10^{-6}$ A/m^2) also evidences the weak bulk pinning at such temperatures.

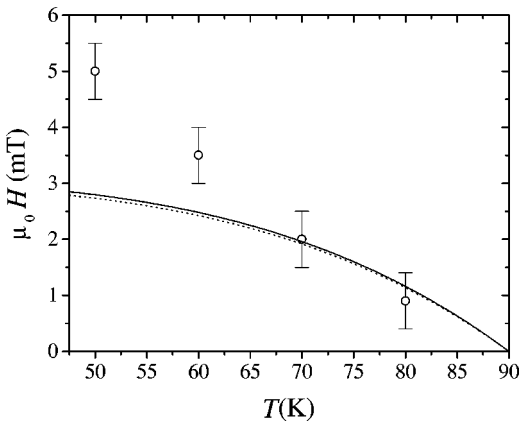

FIG. 2. Experimental H_p (circles) and theoretical $H_{\rm en}$ (lines) within the two-fluid model[9] [$H_{c1}\propto\lambda^{-2}\propto 1-(T/T_c)^4$]. The solid (dotted) line corresponds to the penetration field for the bar (disk), with $\mu_0 H_{c1}^{\rm bar}(0)\approx 19$ mT, and $\mu_0 H_{c1}^{\rm disk}(0)\approx 16$ mT.

In the absence of pinning, it has been shown[9] that the field for first flux penetration (entrance field) is $H_{\rm en}=H_{c1}\tanh(\sqrt{0.36b/a})$ for bars and $H_{\rm en}=H_{c1}\tanh(\sqrt{0.67b/R})$ for disks. Here b is half the specimen thickness, a is the sample half width, and R the sample radius. Figure 2 presents the theoretical values for $H_{\rm en}$ (lines) and the field where the measured magnetization shows a maximum H_p (circles). (In fact, $H_p\approx H_{\rm en}$ if the sample presents negligible pinning and the microscopic barrier for vortex entrance can be neglected, otherwise H_p should be greater than the theoretical $H_{\rm en}$ described above.) In order to compare the data, we used $b=d/2=0.04$ and $a=0.9$ (or $R=1.22$) in $H_{\rm en}$ for the bar (disk) ($a=0.9$ corresponds to half of the sample's smaller transverse dimension and $R=1.22$ to an effective radius of a disk with the same area as the sample). Assuming $H_{c1}(T)=H_{c1}(0)[1-(T/T_c)^4]$, i.e., the two-fluid model, and taking $T_c=90$ K, we found good agreement at $T=70$ K and $T=80$ K by using $\mu_0 H_{c1}(0)\approx 19$ mT (16 mT) for the bar (disk). This gives good estimates for the sample's lower critical field at $T=0$. However, the experimental points at lower temperatures ($T=50$ K and 60 K) do not fit the estimated $H_p(T)$ dependence.

III. NUMERICAL METHOD

In order to calculate the dependence of the magnetization on the external field, we employed a numerical method recently developed for bars and disks of any aspect ratio,[9,13,14] considering an appropriate $E(j)$ relation for the superconducting mixed state (E is the electric field and j the current density). This method is briefly described below.

Taking the external-field direction (y axis) along the specimen thickness, it has been shown that, starting from $\mu_0 \boldsymbol{j}=\boldsymbol{\nabla}\times\boldsymbol{B}$, $\boldsymbol{\nabla}\times\boldsymbol{E}=-\partial\boldsymbol{B}/\partial t$, and a constitutive relation $\boldsymbol{E}$

$=E(j)\mathbf{j}/j$, one obtains the following equation of motion for the current density

$$\mu_0 \frac{dj(\mathbf{r},t)}{dt} = \int dr' \int dy' Q^{-1}(\mathbf{r},\mathbf{r}') \left(E[j(\mathbf{r}',t)] + \frac{dA_a}{dt} \right), \tag{1}$$

where $\mathbf{r}=(x,y)$ (bar) or $\mathbf{r}=(\rho,y)$ (disk), the applied magnetic field B_a is along y, and $A_a=-xB_a$ (or $A_a=-\rho B_a/2$) is the vector potential of B_a. The current flows along $\hat{z}$ (or $\hat{\phi}$), with the vector potential parallel to it; both the quantities do not depend on z (or on the angle ϕ). The integral kernel $Q(\mathbf{r},\mathbf{r}')$ may be evaluated by integrating the three-dimensional (3D) kernel $Q_{3D}(\mathbf{r},\mathbf{r}')=1/(4\pi|\mathbf{r}-\mathbf{r}'|)$ over z' (or over ϕ) for the bar (disk). The inverse kernel $Q^{-1}(\mathbf{r},\mathbf{r}')$ is related to the kernel Q by

$$\int d^2r'' Q^{-1}(\mathbf{r},\mathbf{r}'') Q(\mathbf{r}'',\mathbf{r}') = \delta(\mathbf{r}-\mathbf{r}'). \tag{2}$$

To account for the local-equilibrium flux-line lattice, a given relation $\boldsymbol{H}=H(B)\boldsymbol{B}/B=\partial F/\partial \boldsymbol{B}$ should be considered in order to calculate $\boldsymbol{j}_H=\boldsymbol{\nabla}\times\boldsymbol{H}$.[9] This $\boldsymbol{j}_H$ is the current density that drives the vortices.[12] The electric field thus depends on j_H and the constitutive relation $E(j)$ becomes $E=E(j_H,B)$.[9]

If one maps the specimen cross section onto a discrete grid of points, the above equations can be numerically evaluated by time integration of the equation of motion for j at each grid point. It is useful to take into account the symmetry of the current density, i.e., $j(x,y)=-j(-x,y)=j(x,-y)=-j(-x,-y)$ for a bar in an external field parallel to $\hat{y}$ [and equivalently, $j(\rho,-y)=j(\rho,y)$ for the disk]. This permits us to consider only one quarter of the specimen cross section to obtain higher numerical accuracy. The calculated quantities are normalized, i.e., the lengths are in units of a (or R), $H\rightarrow H/H_{c1}$, $j\rightarrow aj/H_{c1}$ (or Rj/H_{c1}), and $m\rightarrow m/(La^2H_{c1})$ [or $m/(R^3H_{c1})$] for the bar (disk), where L is the longer transverse dimension of the specimen. (Our sample exhibits $L\approx 2.6$ mm, but in our calculation we used $L\approx 2$ mm that yields better agreement with the measured virgin magnetization. Interestingly, a rectangular plate in the fully penetrated critical state in perpendicular field exhibits $m\propto L-2a/3\approx 2$ mm.)

IV. RESULTS AND DISCUSSION

We chose a grid with 25×4 points in one quarter of the sample cross section. The calculation was performed for a disk with $R=1.22$ mm (which gives the same area as that of the actual sample) and for a bar with half width $a=0.9$ mm (the shorter transverse dimension of our sample is about 1.8 mm), both with half thicknesses of $b=0.04$ mm. The numerics was performed by using $\mathbf{E}(\boldsymbol{j}_H,\mathbf{B})=\rho_e(j_H,B)\boldsymbol{j}_H$, where[9]

$$\rho_e(j,B)=\rho_0 B \frac{|j/j_c|^\sigma}{1+|j/j_c|^\sigma}, \tag{3}$$

for several values of the parameters σ, ρ_0, and j_c (the critical-current density). This expression for a generalized resistivity yields flux flow and flux creep when $j \gg j_c$ and $j \ll j_c$, respectively.[9] In the case where $j_c\rightarrow 0$ one gets $\rho_e=\rho_0 B$, which is the Bardeen-Stephen flux-flow model.[22]

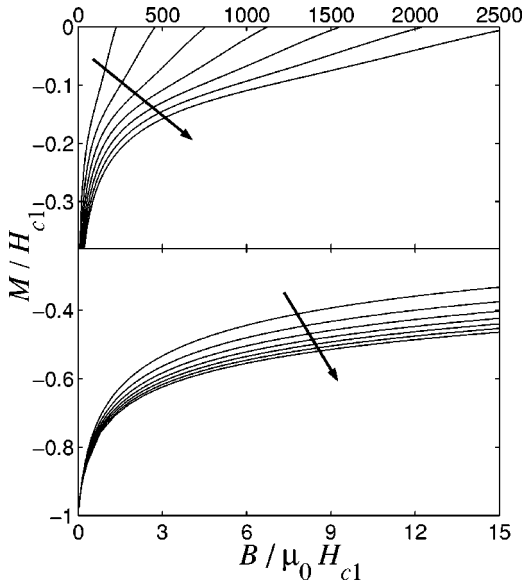

FIG. 3. Dependence on B of $M=B-H$ obtained from the Clem-Hao model for $\kappa=20,30,40,50,60,70$, and 80 (the arrows indicate the direction of increasing κ), normalized to H_{c1}. The full range is depicted in the upper set. In the lower set, a magnification for inductions up to $15\mu_0 H_{c1}$ is depicted.

We also considered an equilibrium relation, $\mathbf{H}=H(B)\mathbf{B}/B$, obtained by using the Clem-Hao model.[20] This variational model considers the interaction between vortex cores, in addition to the interactions between fields and currents, but neglects the vortex-lattice structure. The resulting equilibrium relation depends only on the induction B and on the Ginzburg-Landau (GL) parameter κ. The obtained dependence on B of $M=B-H$ is depicted in Fig. 3 for several values of κ. It is observed that M decreases faster as κ is increased. The model can be extended to account for anisotropy when H is parallel to one of the crystal principal axes, by introducing an effective GL parameter $\tilde{\kappa}$ instead of κ, where $\tilde{\kappa}=\kappa\Gamma^{-1/3}$. This model is equivalent to the solution of the GL equations for large value of κ.[23](In what follows, we write $\tilde{\kappa}$ just to state that we are not restricted to the isotropic case.)

We estimated $\tilde{\kappa}$ by looking for the value that gives the best fit for the reversible magnetic moment at each temperature, considering the case $j_c=0$. This yields a decreasing $\tilde{\kappa}$ as the temperature increases from 50 K to 80 K. Notice that the external-field range is different at each temperature studied, e.g., $|B_a|<10$ mT at 80 K, $|B_a|<50$ mT at 70 K, and $|B_a|<150$ mT at 50 K and 60 K. This may affect the estimated $\tilde{\kappa}$, since quantum and thermal fluctuations of vortices strongly contribute to the mixed-state magnetization at high fields.[24–27]

In order to better adjust the numerical results to the experimental hysteresis, a bulk critical current depending monotonically on the local induction B was also taken into

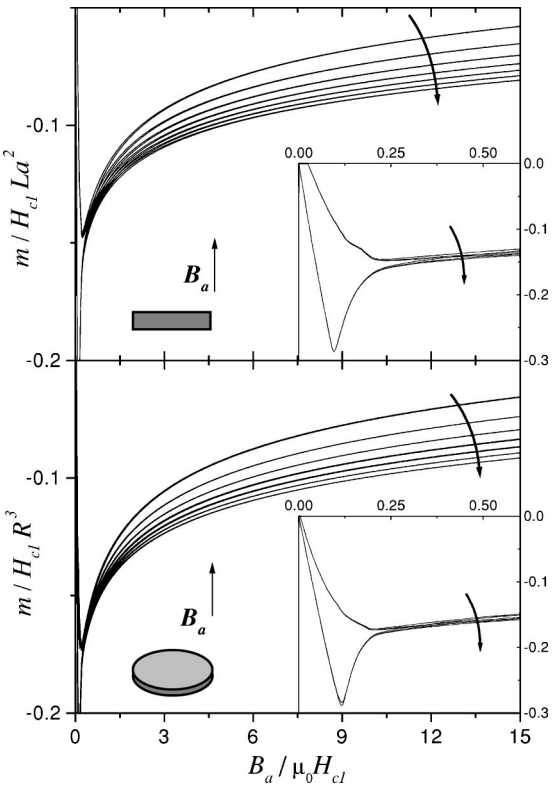

FIG. 4. Numerical magnetic moment considering $j_c=0$, for the bar (top) and the disk (bottom) (with dimensions given in the text), considering the Clem-Hao model for $\tilde{\kappa}=20$, 30, 40, 50, 60, 70, and 80 (the arrow indicates the direction of increasing $\tilde{\kappa}$). The reversible branch depends strongly on the equilibrium relation. Insets: magnification of the magnetization for $\tilde{\kappa}=20$, 50, and 80, at low fields. The hysteresis does not show observable dependence on $\tilde{\kappa}$.

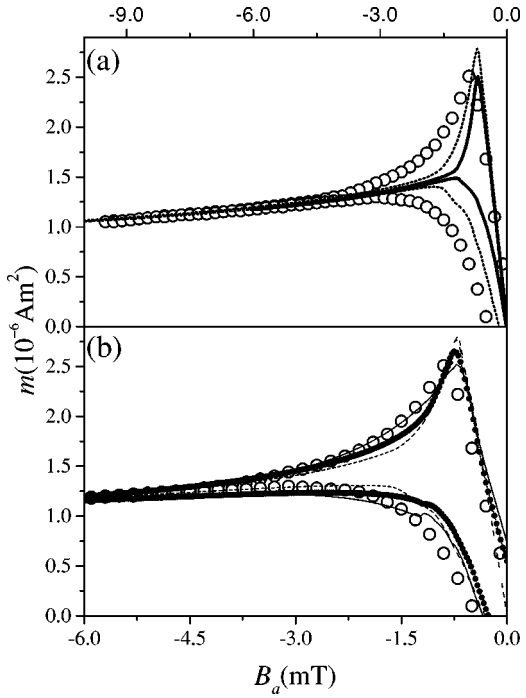

FIG. 5. Magnetic moment at $T=80$ K. The open circles correspond to experimental data. (a) We estimated $\tilde{\kappa}=20\pm5$ and $\mu_0 H_{c1}^{\mathrm{disk}}\approx6$ mT ($\mu_0 H_{c1}^{\mathrm{bar}}\approx9.5$ mT) comparing with the experimental and the numerical reversible branch for $j_c=0$ (solid line for the disk and dashed line for the bar). (b) Numerical curves also considering a monotonic bulk critical current [$j_c(B)=j_{c0}\exp(-\alpha B)$] are depicted in the main figure. The dashed line was obtained by using $j_{c0}\approx6\times10^6$ A/m^2, $\alpha\approx800$ T^{-1}, and $\sigma=20$ (bar). The solid line corresponds to $j_{c0}\approx7.8\times10^6$ A/m^2, $\sigma=20$ and the line with dots to $j_{c0}\approx1.57\times10^7$ A/m^2, $\sigma=2$, both with $\alpha\approx830$ T^{-1} for the disk.

account. We chose $j_c(B)=j_{c0}\exp(-\alpha B)$ since this provides a good fit to the numerical data at 70 K and 80 K, and it avoids parameters in excess.

Magnetization curves for a bar and a disk (top and bottom, respectively), with the dimensions as considered above are shown in Fig. 4 considering $j_c=0$ and $\tilde{\kappa}=20,30,40,50,60,70$, and 80 (the arrow indicates the direction of increasing $\tilde{\kappa}$). In the main set the magnetization is depicted for external fields up to $15H_{c1}$, with the reversible branch strongly dependent on the chosen $\tilde{\kappa}$. Therefore, the reversible magnetization is related to the equilibrium magnetization, decaying faster with decreasing $\tilde{\kappa}$. It is also worth noticing that the difference between two adjacent curves is larger for lower $\tilde{\kappa}$, both for a bar and for a disk. The inset shows a magnification of the data with $\tilde{\kappa}=20,50$, and 80, for $0\leqslant B_a\leqslant0.6\mu_0 H_{c1}$. The hysteretic magnetization is restricted to values of external fields lower than $0.25H_{c1}$ and it does not present a strong dependence on the equilibrium magnetization. We also observed that the reversible branch does not depend on the creep exponent σ, and on ρ_0 in our numerics. The addition of a finite j_c does not affect the reversible branch too; it only increases the hysteresis width and the field where reversibility begins.

Figures 5 and 6 depict the measured (open circles) and numerically calculated (lines) magnetic moments at 80 K and 70 K, respectively. In both figures the numerical magnetization was calculated by considering a finite j_c, except for the lines shown in Figs. 5(a) and 6(a,b), which represent the calculation performed with zero critical current. For both temperatures we found good agreement between experimental and numerical curves. The reversible branch is well described by the Clem-Hao model with $\tilde{\kappa}(T=80\ \mathrm{K})=20\pm5$ and $\tilde{\kappa}(T=70\ \mathrm{K})=50\pm5$. The reversible branch is fitted by using $\mu_0 H_{c1}(T=80\ \mathrm{K})\approx6$ mT and $\mu_0 H_{c1}(T=70\ \mathrm{K})\approx9.5$ mT for the disk, and $\mu_0 H_{c1}\approx7.5$ mT and $\mu_0 H_{c1}(T=70\ \mathrm{K})\approx12$ mT for the bar [see Figs. 5(a) and 6(a) where the reversible magnetization is depicted enlarged]. Also, the geometric barrier greatly influences the hysteresis, more strongly at $T=80$ K than it does at 70 K, as can be seen in Figs. 5(a) and 6(b). As Figs. 5(c) and 6(c) show, a better fit is obtained when a small bulk critical current is considered, yielding calculated H_p greater than the geometric barrier H_{en}.

The critical-current value estimated depends on the exponent σ of the $E(j)$ relation [Eq. (3)]. We used $\sigma=20$, 4, and 2 that are related to weak, strong, and very strong (almost ohmic) flux creep, respectively. The comparison between ex-

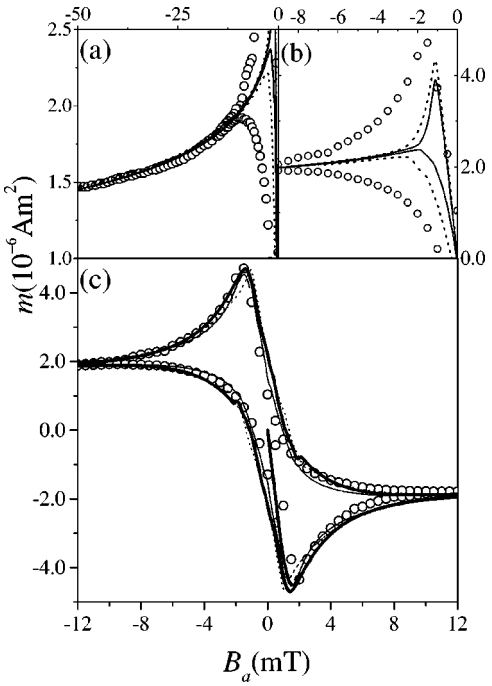

FIG. 6. Data at $T=70$ K. (a) The comparison between experimental (open circles) and numerical loops for $j_c=0$ (solid line for the disk and dashed line for the bar) shows $\tilde{\kappa}=50\pm5$ and $\mu_0 H_{c1}^{\mathrm{disk}}\approx 9.5$ mT ($\mu_0 H_{c1}^{\mathrm{bar}}\approx 12$ mT). (b) Magnification of the loops shown in (a) at low fields. This figure shows that the geometric barrier strongly affects the hysteresis at this temperature also. (c) Experimental (open circles) and numerical data obtained by using finite j_c. The thick line (thin line) corresponds to $j_{c0}\approx 2.5\times10^7$ A/m^2 ($j_{c0}\approx 1\times10^8$ A/m^2), $\alpha\approx 420$ T^{-1}, with $\sigma=20$ ($\sigma=2$) for the disk. The dashed line is for the bar considering $j_{c0}\approx 2\times10^7$ A/m^2, $\alpha\approx 340$ T^{-1}, and $\sigma=20$.

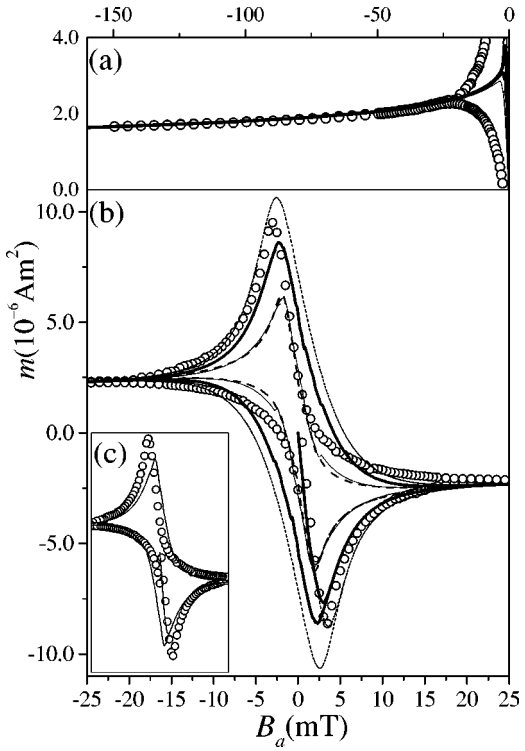

FIG. 7. Same as Fig. 5 but at $T=60$ K with $\tilde{\kappa}=70\pm5$ and $\mu_0 H_{c1}^{\mathrm{disk}}\approx 12$ mT. We show several numerical curves for the disk compared with experimental data (b) as follows: $j_{c0}\approx 1.6\times10^7$ A/m^2, $\sigma=20$ (thin line); $j_{c0}\approx 4.0\times10^7$ A/m^2, $\sigma=20$ (thick line); $j_{c0}\approx 3.6\times10^8$ A/m^2, $\sigma=4$ (dotted line) and $j_{c0}\approx 1.6\times10^8$ A/m^2, $\sigma=2$ (dashed line), all of them were calculated by using $\alpha\approx 325$ T^{-1}. (c) Experimental (circles) and numerical data for the bar considering $j_{c0}\approx 5.3\times10^7$ A/m^2, $\sigma=20$, $\alpha\approx 270$ T^{-1}. (a) Magnification of the reversible branch, where the numerical loops with $j_c=0$ (thick line for the disk and dotted line for the bar) are compared with the experimental points.

perimental and numerical magnetizations does not allow us to determine the creep exponent, since good agreement can be found with different σ by varying j_c. At $T=80$ K [Fig. 5(c)], numerical data for the bar was evaluated by using $j_{c0}\approx 6\times10^6$ A/m^2, $\alpha\approx 800$ T^{-1}, and $\sigma=20$ (dashed line). The same figure shows the cases $j_{c0}\approx 7.8\times10^6$ A/m^2, $\sigma=20$ (solid line) and $j_{c0}\approx 1.57\times10^7$ A/m^2, $\sigma=2$ (line with solid dots), both with $\alpha\approx 830$ T^{-1} for the disk. The values for the disk and the bar present reasonable agreement, and the fitted critical current is larger when a smaller creep exponent is chosen, as it should be expected. Moreover, the very low critical-current values (10^{-6}–10^{-5} times the magnitude of the depairing current) indicate the major role of the geometric barrier at this temperature [see, for instance, Fig. 5(a), where the numerically obtained magnetization with zero-bulk critical current is compared with experimental data]. The critical current estimated at $T=70$ K is also very low. In Fig. 6(c) the magnetic moment at 70 K is shown compared with several numerical curves considering: $j_{c0}\approx 2\times10^7$ A/m^2, $\alpha\approx 340$ T^{-1} with $\sigma=20$ (dashed line) for the bar; $j_{c0}\approx 2.5\times10^7$ A/m^2, $\sigma=20$ (thick line), and $j_{c0}\approx 1\times10^8$ A/m^2, $\sigma=2$ (thin line), both with $\alpha\approx 420$ T^{-1} for the disk. These critical-current values are three and six times greater than those estimated at $T=80$ K for $\sigma=20$ and $\sigma=2$, respectively, but still much smaller than the depairing current.

Good agreement between experimental and numerical data is also found for the reversible branch at $T=50$ K and $T=60$ K, as depicted in Figs. 7(a) and 8(a), where the thick and the dotted lines represent the magnetization calculated with zero critical current for the disk and the bar, respectively [the thin line in Fig. 8(a) is for finite j_c, corresponding to the thick line in Fig. 8(b)]. We estimate $\mu_0 H_{c1}$ (60 K) ≈ 12 mT and $\mu_0 H_{c1}$ (50 K)≈ 14 mT for the disk, and $\mu_0 H_{c1}$ (60 K)≈ 15 mT and $\mu_0 H_{c1}$ (50 K)≈ 17.5 mT for the bar. For both the disk and the bar we also find that $\tilde{\kappa}$ (60 K)$\approx 70\pm5$ and $\tilde{\kappa}$ (50 K)$\approx 80\pm5$. However, the numerical magnetization hysteresis does not show the same agreement that was observed at higher temperature.

In Fig. 7(b), experimental points measured at $T=60$ K are compared with numerical ones obtained with $\alpha\approx 325$ T^{-1} for the disk. The various curves were calculated for: $j_{c0}\approx 1.6\times10^7$ A/m^2, $\sigma=20$ (thin line); $j_{c0}\approx 4.0\times10^7$ A/m^2, $\sigma=20$ (thick line); $j_{c0}\approx 3.6\times10^8$ A/m^2, $\sigma=4$ (dotted line), and $j_{c0}\approx 1.6\times10^8$ A/m^2, $\sigma=2$ (dashed line). (One may notice that the thin and the dashed lines are

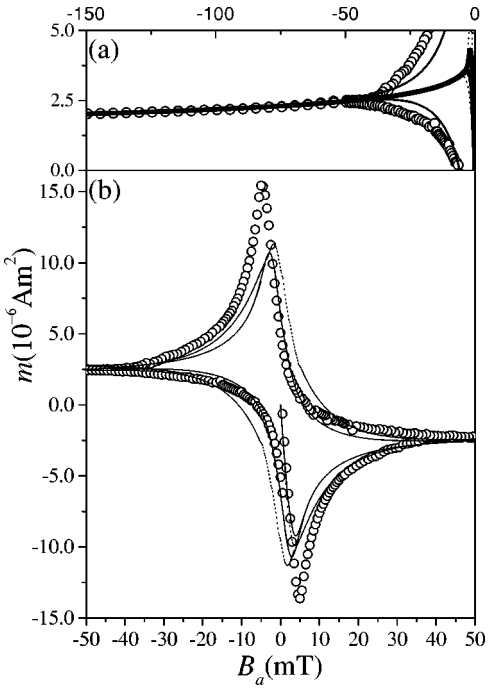

FIG. 8. Same as Fig. 5 but at $T=50$ K with $\tilde{\kappa}=80\pm5$ and $\mu_0 H_{c1}^{\mathrm{disk}}\approx 14$ mT ($\mu_0 H_{c1}^{\mathrm{bar}}\approx 17.5$ mT). (b) Numerical data for the bar (thin line, $\sigma=20$, $j_{c0}\approx 8\times10^7$ A/m^2, $\alpha\approx 110$ T^{-1}) and for the disk ($\sigma=2$, $j_{c0}\approx 5.6\times10^8$ A/m^2, $\alpha\approx 140$ T^{-1}) are compared with experiment (circles). (a) Numerical data considering $j_c=0$ (thick line for the disk and dotted line for the bar) and finite j_c (thin line) corresponding to the thick line in (b). Good agreement is seen in the reversible branch between experimental and numerical curves as observed at higher temperature.

almost identical.) It can be observed that the numerical curves that agree with the experimental hysteresis at low external fields ($|B_a|<2$ mT), which are the thin and dashed lines, present lower H_p (the field at which the magnetization is maximum) compared with the experimental H_p. On the other hand, for higher j_{c0} (or larger σ) values (thick and dotted lines), the numerical curves show better agreement at $B_a>\mu_0 H_p$, although they are larger than the experimental data at low fields. A comparison with the numerics for the bar is shown in the lower inset, considering $j_{c0}\approx 5.3\times10^7$ A/m^2, $\sigma=20$, and $\alpha\approx 270$ T^{-1}, which presents the same features observed in the numerics for the disk, i.e., the numerical hysteresis is larger at low external fields and presents smaller H_p as compared to the experimental data. The same behavior is also observed at $T=50$ K, as shown in Fig. 8(b), where numerical data is depicted for the bar with $\sigma=20$, $j_{c0}\approx 8\times10^7$ A/m^2, and $\alpha\approx 110$ T^{-1} (thin line), and for the disk with $\sigma=2$, $j_{c0}\approx 5.6\times10^8$ A/m^2, and $\alpha\approx 140$ T^{-1} [thick and thin lines in Figs. 8(b) and 8(a), respectively].

The reason for the difference observed in the numerical and experimental hysteresis at 50 K and 60 K is not clear. We outline two possible scenarios that could explain this.

(a) The flux penetration involves critical current or creep exponent σ that depends nonmonotonically on B. A weaker (stronger) critical current or creep exponent at low (high) B would account for narrower (wider) hysteresis near $B_a \ll \mu_0 H_p (B_a \geqslant \mu_0 H_p)$.

(b) Another type of vortex-surface barrier is acting on the specimen.[28] This is an interesting picture, since vortices may jump this surface barrier at high temperature and the geometric barrier becomes more relevant. At lower temperatures, vortex jumping through the surface would be less probable and this surface barrier could be more significant than the geometric barrier. This picture requires to consider the microscopic vortex penetration in detail.

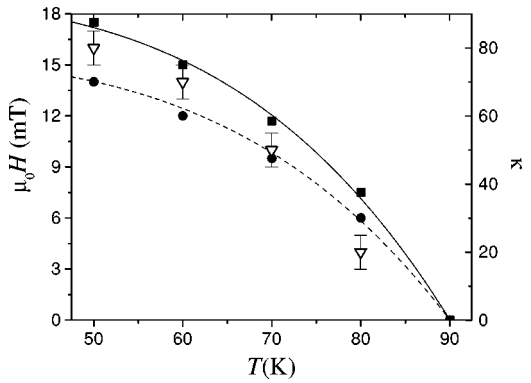

FIG. 9. Temperature dependences of $\tilde{\kappa}$ (open triangles) and H_{c1} (solid symbols) obtained from the comparison between experimental and numerical curves. The circles (squares) and the dashed (solid) lines correspond to H_{c1} extracted from the disk (bar) and to the expression $\mu_0 H_{c1}=15.5(1-t^4)$ mT [$\mu_0 H_{c1}=19(1-t^4)$ mT], where $t=T/T_c$.

The temperature dependence of the estimated H_{c1} (squares compared with the bar and circles compared with the disk) and $\tilde{\kappa}$ is depicted in Fig. 9. Also shown are the relations $\mu_0 H_{c1}^{\mathrm{bar}}(T)=19[1-(T/90)^4]$ mT (solid line) and $\mu_0 H_{c1}^{\mathrm{disk}}(T)=15.5[1-(T/90)^4]$ mT (dashed line). This indicates $H_{c1}(0)\approx 15$ mT–20 mT for our single crystal.

Special attention must be paid to the temperature dependence of $\tilde{\kappa}$. Applying their model, Hao and co-authors found that $\tilde{\kappa}$ increases as temperature increases.[20] This increase in κ was explained as resulting from thermal fluctuations of vortices,[25] which give an additional contribution to the magnetization.[24] They obtained $\tilde{\kappa}$ by fitting theoretical expressions to experimental data at external fields above 0.1 T, neglecting demagnetization effects. (Martinez *et al.*[26] also showed that quantum fluctuations of vortices[27] are present in the magnetization dependence on B.) However, the contribution to the magnetization from fluctuations of vortices is small at low external-fields. This suggests that the external-field range in our measurements could influence the determination of $\tilde{\kappa}$, since we have $|B_a|<150$ mT at $T\leqslant 60$ K, $|B_a|<50$ mT at $T=70$ K, and $|B_a|<10$ mT at $T=80$ K. Therefore, at $T\leqslant 70$ K we cannot assure that the magnetic induction is low enough to neglect fluctuations of vortices. This could be contributing to the magnetization, which would explain the higher $\tilde{\kappa}$ found at lower T.

V. SUMMARY

We studied the magnetization dependence on the external field by comparison of experimental results with numerical magnetization. The calculated magnetization carefully considers the sample dimensions, the external-field direction, the equilibrium magnetization, given by the Clem-Hao model, and an $E(j)$ relation that yields flux creep. We found good agreement in the reversible branch between experimental and numerical data at the external-field range studied. This allowed us to estimate the lower critical field [$\mu_0 H_{c1}(0) \sim 15-20$ mT] and its temperature dependence at the studied field range. The decreasing $\tilde{\kappa}$ for increasing temperature might be related to the different external-field range considered, so the high values found at $T<70$ K could be influenced by the contribution to the magnetization from fluctuation of vortices, which we did not consider in the calculations.

The hystereses also show good agreement with the numerics at 70 K and 80 K, when a bulk critical current is taken into account. This yields information about the magnitude of the critical current, which is around $10^{-6}-10^{-5}$ times the depairing current, depending on the creep exponent. (Unfortunately, we could not estimate j_c and σ independently through direct comparison between numerical and magnetization loops.) Therefore, the geometric barrier is quite important for understanding the hysteresis at these temperatures. In fact, the hysteresis at 80 K is dominated by the geometric barrier. At 50 K and 60 K, the numerical data does not fit the experimental hysteresis as well as it fitted at 70 K and 80 K, if j_c and σ were considered to depend monotonically on B. The reason for this is not clear, but we suggest two possible explanations: a nonmonotonic dependence of the critical current or the creep exponent on the local induction; another type of barrier for vortex penetration which would be more pronounced than the geometric barrier below 70 K, but would be overcome by thermal fluctuations at high temperatures, e.g., $T \geqslant 70$ K. Further studies are under way and will be published elsewhere.

ACKNOWLEDGMENTS

We would like to thank Gilson M. Carneiro for helpful discussions. This work was supported by Brazilian Science Agencies CNPq and FACEPE.

*Electronic address: leon@df.ufpe.br

[1] C.P. Bean, Phys. Rev. Lett. **8**, 250 (1962).
[2] C.P. Bean and J.D. Livingston, Phys. Rev. Lett. **12**, 14 (1964).
[3] Y.B. Kim and A.R. Strnad, Phys. Rev. Lett. **9**, 306 (1962).
[4] J.R. Clem, in *Low Temperature Physics*, edited by K.D. Timmerhaus, W.J. O'Sullivan, and E.F. Hammel (Plenum, New York, 1974), Vol. 3, p. 102.
[5] C.C.d.S. Silva and J. Albino Aguiar, Physica C **354**, 232 (2001).
[6] C.C.d.S. Silva, L.R.E. Cabral, and J. Albino Aguiar, Phys. Rev. B **63**, 134526 (2001).
[7] W.T. Norris, J. Phys. D **3**, 489 (1970).
[8] E.H. Brandt and M. Indenbom, Phys. Rev. B **48**, 12 893 (1993).
[9] E.H. Brandt, Phys. Rev. B **59**, 3369 (1999); **60**, 11 939 (1999).
[10] E. Zeldov, A.I. Larkin, V.B. Geshkenbein, M. Konczykowski, D. Majer, B. Khaykovich, V.M. Vinokur, and H. Shtrikman, Phys. Rev. Lett. **73**, 1428 (1994).
[11] M. Benkraouda and J.R. Clem, Phys. Rev. B **53**, 5716 (1996).
[12] R. Labusch and T.B. Doyle, Physica C **290**, 143 (1997).
[13] E.H. Brandt, Phys. Rev. B **54**, 4246 (1996).
[14] E.H. Brandt, Phys. Rev. B **58**, 6506 (1998).
[15] G. Blatter, M.V. Feigel'man, V.B. Geshkenbein, A.I. Larkin,and V.M. Vinokur, Rev. Mod. Phys. **66**, 1125 (1994).
[16] C. J. van der Beek, Ph.D. thesis, Free University at Leiden, 1992.
[17] L.R.E. Cabral, D.A. Landinez Tellez, P.H. Kes, and J. Albino Aguiar, J. Magn. Magn. Mater. **177-181**, 513 (1998).
[18] R.I. Khasanov, Yu.I. Talanov, W. Assmus, and G.B. Teitel'baum, Phys. Rev. B **54**, 13 339 (1996).
[19] N. Morozov, E. Zeldov, M. Konczykowski, and R.A. Doyle, Physica C **291**, 113 (1997).
[20] Z. Hao, J.R. Clem, M.W. Mc Elfresh, L. Civale, A.P. Malozemoff, and F. Holtzberg, Phys. Rev. B **43**, 2844 (1991).
[21] Y.K. Huang, K. Kadowaki, M.J.V. Menken, J.M. Li, K. Bakker, A.A. Menovsky, J.J.M. Franse, G.F. Bastin, H.J.M. Heijligers, H. Barten, J. van den Berg, R.A. Zacher, and H.W. Zandbergen, Physica C **152**, 431 (1988).
[22] J. Bardeen and M.J. Stephen, Phys. Rev. **140**, A1197 (1965).
[23] E.H. Brandt, Phys. Rev. Lett. **78**, 2208 (1997).
[24] L.N. Bulaevskii, M. Ledvij, and V.G. Kogan, Phys. Rev. Lett. **68**, 3773 (1992).
[25] V.G. Kogan, M. Ledvij, A.Y. Simonov, J.H. Cho, and D.C. Johnston, Phys. Rev. Lett. **70**, 1870 (1993).
[26] J.C. Martinez, P.J.E.M. van der Linden, L.N. Bulaevskii, S. Brongersma, A. Koshelev, J.A.A.J. Perenboom, A.A. Menovsky, and P.H. Kes, Phys. Rev. Lett. **72**, 3614 (1994).
[27] L.N. Bulaevskii and M.P. Maley, Phys. Rev. Lett. **71**, 3541 (1993).
[28] A detailed discussion on surface barriers is given by E.H. Brandt, Rep. Prog. Phys. **58**, 1465 (1995).